JOURNAL OF GEOPHYSICAL RESEARCH, VOL. 104, NO. D17, PAGES 21,471–21,485, SEPTEMBER 20, 1999

Simulation of carbon monoxide transport during April 1994

G. S. Faluvegi, K. Alapaty,[1] and H. G. Reichle Jr.
Department of Marine, Earth, and Atmospheric Sciences, North Carolina State University, Raleigh

R. Mathur
Environmental Programs, MCNC-North Carolina Supercomputing Center, Research Triangle Park

S. Raman and V. S. Connors[2]
Department of Marine, Earth, and Atmospheric Sciences, North Carolina State University, Raleigh

Abstract. The Multiscale Air Quality Simulation Platform (MAQSIP) is used to simulate transport of carbon monoxide (CO) as a passive tracer over North America, Europe, and the North Atlantic during the April 1994 Measurement of Air Pollution from Satellites (MAPS) mission. MAQSIP is driven by meteorological fields generated by the Pennsylvania State University/National Center for Atmospheric Research fifth-generation mesoscale model. Model CO surface emissions from biomass burning, fossil fuel combustion, nonmethane hydrocarbon oxidation, oceans, and soils are based on inventories from the Belgian Institute for Space Aeronomy and the Global Emissions Inventory Activity. Predicted CO mixing ratios are vertically weighted for comparison with MAPS observations. The spread in the mission-averaged vertically weighted simulated CO mixing ratios (~38 ppbv, compared to 60 ppbv in the MAPS data) suggests that CO surface emissions significantly affect MAPS observations on a weekly timescale. Good qualitative agreement is found between MAPS observations and model predictions on several temporal and spatial scales. Possible reasons for discrepancies are examined. A simulation without cumulus convection increases CO mixing ratios in the lower model layers and depletes CO above, resulting in a complex pattern of increases and decreases upon vertical weighted integration. Another simulation, which included a diurnal emissions variation, produced significant changes in instantaneous local CO mixing ratios, but had a minimal effect on the mission-averaged MAPS comparisons.

1. Introduction

Carbon monoxide (CO) is one of the most common and widely distributed air pollutants. It is an important atmospheric trace gas for several reasons. CO is toxic to humans [*U.S. Environmental Protection Agency* (*EPA*), 1995] and a precursor to tropospheric ozone (O_3) [*Crutzen*, 1973]. Globally, CO has both a direct radiative effect on the atmospheric energy budget [*Evans and Puckrin*, 1995] and a stronger indirect effect through its interaction with the hydroxyl radical (OH) [*Sze*, 1977]. OH is the primary sink of reduced species in the troposphere, and CO is the primary sink for OH [*Logan et al.*, 1981]. Therefore increased tropospheric CO concentrations hinder the removal of other greenhouse gases and pollutants, such as methane (CH_4) and sulfur dioxide (SO_2). Through its effects on CH_4, CO can also affect stratospheric ozone concentrations [e.g., *Brasseur and Solomon*, 1986]. As a result of these mechanisms, changing CO concentrations can influence global atmospheric chemistry and climate.

Carbon monoxide has large anthropogenic and natural source components, mostly from biomass burning, fossil fuel combustion, and the oxidation of hydrocarbons, and the primary sink of CO is oxidation by OH. The chemical lifetime of CO varies from about a month to about a year. Consequently, CO remains in the atmosphere long enough to be transported great distances from source regions, but not long enough to become uniformly mixed. The result is complex distributions that depend on the magnitudes and distributions of sources and sinks, seasonal variations in atmospheric chemistry, and long- and short-range transport.

Several researchers have examined the importance of transport in understanding CO distributions. Global, multiyear model simulations have been performed to study the sensitivity of large-scale CO distributions to source and sink parameterizations [*Pinto et al.*, 1983] and to the interannual variability of CO transport [*Allen et al.*, 1996]. *Brasseur et al.* [1996] and *Müller and Brasseur* [1995] used a global chemistry and transport model (CTM) to study the distributions, budgets, and trends of various chemical species, including CO. *Doddridge et al.* [1994] studied the effects of transport variability on variations in CO measurements from ground based stations and aircraft. Other research [*Connors et al.*, 1989; *Newell et al.*, 1988] used isentropic back trajectories and detailed investigations of concurrent meteorology to explain CO observations in terms of air parcel histories. These papers demonstrated the important role of large-scale transport, convective-scale transport associated with cold fronts and thunderstorms, and strato-

[1]Also at Environmental Programs, MCNC-North Carolina Supercomputing Center, Research Triangle Park.
[2]Also at NASA Langley Research Center, Hampton, Virginia.

Paper number 1998JD100030.
0148-0227/99/1998JD100030$09.00

spheric detrainment. *Chatfield et al.* [1998] used the Pennsylvania State University/National Center for Atmospheric Research (PSU/NCAR) fifth-generation mesoscale model (MM5) to simulate the transport of CO from biomass burning in Africa and South America over the tropical Atlantic. *Wang et al.* [1996] also used MM5 to simulate case studies of CO transport in the vicinity of a tropical mesoscale convective system and a midlatitude squall line. Regional CO budget studies have emphasized the role of convective vertical transport in the tropics [*Pickering et al.*, 1992; *Thompson et al.*, 1997] and in the central United States [*Luke et al.*, 1992; *Thompson et al.*, 1994].

Owing to the complex CO distributions, measurements made over large areas in short time periods are only practical from space-borne remote sensors. The Measurement of Air Pollution from Satellites (MAPS) instrument is a gas-filter radiometer that has taken such measurements during four space shuttle missions [*Reichle et al.*, 1986, 1990, this issue]. A further reason for studying CO transport is to help understand such column-averaged observations by providing a simulation of the three-dimensional motions and instantaneous distributions of the gas. This type of modeling will continue to be a useful tool for analyzing future observations made by the Measurement of Pollution in the Troposphere (MOPITT) instrument as part of the NASA Earth Observing System (EOS) [*Drummond and Mand*, 1996].

The objectives of the current study are (1) to simulate the transport of CO during the April 1994 MAPS mission using a multiscale air quality model, (2) to compare model simulations with MAPS data, and (3) to study how convective transport and diurnal variation in CO emissions affect the model simulation. Our simulations benefit from assimilated meteorology, allowing modeling of specific time periods with realistic transport of CO. To our knowledge, this is the first modeling study to use a vertically weighted integration [*Reichle et al.*, this issue; *Pougatchev and Sachse*, 1997] to compare simulated CO mixing ratios with MAPS data.

2. Description of Models

In this study, we used the Pennsylvania State University/National Center for Atmospheric Research (PSU/NCAR) fifth-generation mesoscale modeling system, version 1 (MM5) [*Grell et al.*, 1995; S. Chen et al., PSU/NCAR mesoscale modeling system tutorial class notes, Mesoscale and Microscale Meteorology Division, NCAR, 1996, available at http://www.mmm.ucar.edu/mm5/tutorial-notes.html] to generate meteorological fields, which were used to drive a CTM and simulate CO transport. The Multiscale Air Quality simulation Platform (MAQSIP) [*Byun et al.*, 1995; *Odman and Ingram*, 1996] is the CTM used to perform the CO simulations.

2.1. Brief Description of MM5

MM5 uses an Arakawa-Lamb B-staggered grid. Model simulations were performed in nonhydrostatic mode. During the model simulation, four-dimensional data assimilation was used to nudge predicted variables toward meteorological observations. The planetary boundary layer (PBL) was modeled using a modified Blackadar scheme [*Blackadar*, 1976; *Zhang and Anthes*, 1982] for convective conditions, and K theory for other stability regimes. The Anthes-Kuo cumulus parameterization [*Anthes*, 1977; *Kuo*, 1974] was used to model cloud processes.

2.2. Brief Description of MAQSIP

The same grid configuration used in MM5 was used to perform CTM simulations of CO. The governing equation for the chemical species in MAQSIP is

$$\frac{\partial \sqrt{\gamma}\bar{c}}{\partial t} + \frac{\partial \sqrt{\gamma}\overline{c v_j}}{\partial x_j} + \frac{\partial}{\partial x_j}\left[-\sqrt{\gamma}\bar{\rho}K_{jj}\frac{\partial}{\partial x_j}\frac{\bar{c}}{\bar{\rho}}\right] = \sqrt{\gamma}R + \sqrt{\gamma}S \quad (1)$$

where c is the CO concentration; γ is the determinant of the metric tensor, which accounts for the specific coordinate system; x_j are the three spatial coordinates ($j = 1, 2, 3$); v_j are the corresponding velocities; ρ is the density of the air/CO mixture; K_{jj} is the component of the diffusivity tensor in the $x_j \cdot x_j$ direction; R is the chemical formation or loss rate; and S is the source/sink term.

To treat CO as a passive tracer, the chemistry term in the governing equation was neglected. This assumption is justified because the time period of the simulation (about 10 days) was significantly shorter than the typical chemical lifetime of CO in the atmosphere. Consequently, the source/sink term consisted of CO surface emissions as described in section 3.1 and no sink due to reaction with hydroxyl. The fact that the April Northern Hemisphere OH sink is closer to its (winter) minimum than its (summer) maximum strengthens the passive tracer assumption. As is evident in the third term of (1), the turbulent diffusion was parameterized using K theory. The vertical transport of CO due to cumulus convection was parameterized by a cloud scheme described by *Chang et al.* [1987], and both vertical and horizontal advection used the Bott scheme [*Bott*, 1989a, b].

3. Description of Numerical Simulations

We ran MM5 and MAQSIP for the time period from 1200 UTC March 30 through 1200 UTC April 19, 1994. This period includes the MAPS mission and 10 days prior to the mission. The initial condition for March 30 was a uniform CO mixing ratio of 100 parts per billion by volume (ppbv). In order to improve on this uniform initial condition, the simulated mixing ratio field after the first 10 days of simulation was used as the initial condition for the MAPS time period. The spatial domain is depicted in Figure 1. At the edge of the domain, CO was free to advect outward, and air advecting inward carried a constant CO mixing ratio of 100 ppbv. Four-dimensional data assimilation was used to nudge wind fields (throughout the model atmosphere) and temperature and humidity (above the PBL) toward observed values. Because of the computational constraints of this large spatial domain, a horizontal resolution of 100 km was used. There are 15 vertical layers from 100 hPa (the top of the model atmosphere) to the terrain surface, bounded by the 16 sigma surfaces: $\sigma = \{0.0, 0.1, 0.2, 0.3, 0.4, 0.5, 0.6, 0.7, 0.78, 0.84, 0.89, 0.93, 0.96, 0.98, 0.99, 1.00\}$. The lowest model layer thickness is about 76 m, and there are typically five or six layers in the lowest 1 km of the atmosphere.

The meteorological variables from MM5 and the CO mixing ratios from MAQSIP were output each hour for each of the 15 vertical levels and each of the 120×51 horizontal grid squares. We viewed the output in horizontal and vertical cross sections, time series, animations, and individually. We performed three simulations: CASE1, which includes cumulus convection and CO emissions that are uniform in time; CASE2, which is identical to CASE1 except that cloud processes are turned off in

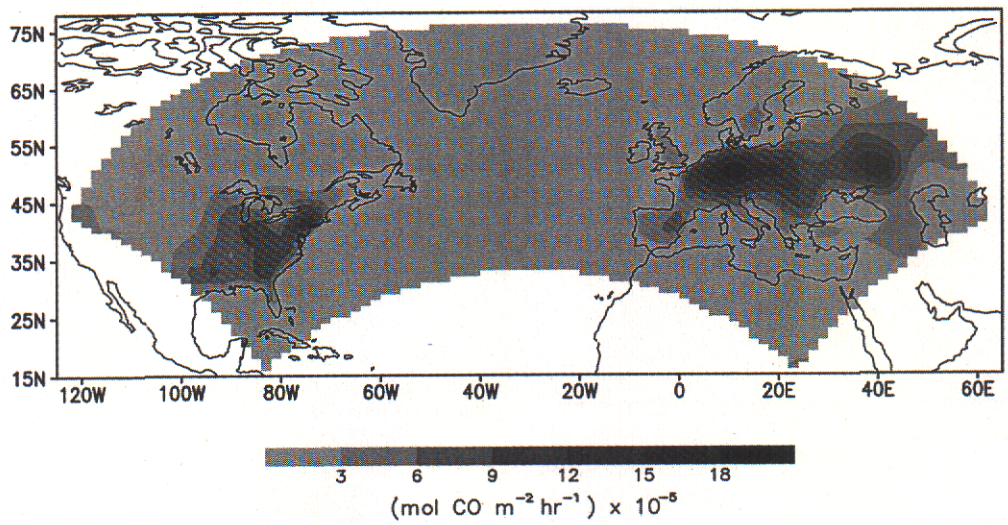

Figure 1. Prescribed CO emissions in mol CO m^{-2} h^{-1} ($\times 10^{-5}$) released in the lowest model layer. In CASE1 and CASE2, CO was emitted at a constant rate. In CASE3 a mass-conserving diurnal variation in emissions was applied to these values.

order to study the role of clouds in CO transport; and CASE3, which differs from CASE1 only in its CO emissions rate, which varies diurnally.

3.1. Model CO Emissions

Model CO emissions were released in the lowest model layer. The spatial distribution of emissions was based upon published estimates as described below. We obtained 5° × 5° gridded anthropogenic, biomass burning, soil, and ocean CO emissions from a global trace gas emissions inventory from the Belgian Institute for Space Aeronomy (IAS). These inventories are described in detail by *Müller* [1992]. The anthropogenic component includes fossil fuel burning, waste disposal, metallurgy, petroleum refining, and ammonia production, and is largely based on data from the Organization for Economic Cooperation and Development [*OECD*, 1989]. These sources were spatially distributed based on population density and location of industrial and mining activities and temporally distributed based on seasonal variation of fossil fuel use and temperature dependence of vehicle emissions. The biomass burning source includes the burning of savanna and forests as well as wood fuel and agricultural waste burning. Emissions over water were set to a constant value representative of estimates from the IAS data set (2.0×10^{-6} mol CO m^{-2} h^{-1}). CO sources from nonmethane hydrocarbon (NMHC) oxidation were parameterized from 1990 natural volatile organic compound (NVOC) 1° × 1° emissions estimates from the Global Emissions Inventory Activity (GEIA) database [*Guenther et al.*, 1995]. The conversion factors from NVOC to CO emissions were the same as those used by *Allen et al.* [1996] and are appropriate for the United States/European domain (2.5 mol CO/mol isoprene and 0.8 mol CO/mol monoterpene). The various emissions components described above were summed, and the total surface emissions are shown in Figure 1. Emission rates vary from near zero in parts of North Africa to about 2×10^{-4} mol CO m^{-2} h^{-1} in urban and industrial centers and in rainforests of the Yucatán Peninsula.

The only significant omitted CO source is from methane oxidation. While all sources described above are emitted in the lowest model layer, a methane oxidation source would be a three-dimensional source, which is dependent upon [OH], [CH_4], and temperature. *Logan et al.* [1981] estimate the methane oxidation source as 22% of the total Northern Hemisphere CO source. An average of other published estimates confirms this, placing the global methane oxidation source at about 1/4 of the total [*Müller and Brasseur*, 1995; *Logan et al.*, 1981; *Allen et al.*, 1996; *Seiler and Conrad*, 1987; *Pacyna and Graedel*, 1995; *Volz et al.*, 1981; *Khalil and Rasmussen*, 1990.]

Significant uncertainties are associated with any estimate of CO emissions. The global IAS biomass burning and ocean CO flux estimates and the GEIA NMHC flux estimates are uncertain by a factor of 3 or more [*Müller*, 1992; *Guenther et al.*, 1995]. Fortunately, CO fluxes in our model domain are dominated by anthropogenic sources, which are more certain. For example, the global technological source term in the *Müller* [1992] budget has a range of about 300–450 Tg/yr (J.-F. Müller, personal communication, 1998). Over the United States the model emissions are in reasonable qualitative and quantitative agreement with 1994 U.S. Environmental Protection Agency (EPA) estimated emissions, which suggest an average anthropogenic CO flux of about 4.6×10^{-5} mol CO m^{-2} h^{-1} [*U.S. EPA*, 1995].

In CASE1 and CASE2, emissions were released at a constant rate. In CASE3 a diurnal pattern was imposed upon the emissions rate. The time-varying pattern of observed CO area sources over land was averaged for 5 days over the eastern United States, using data from the 1990 U.S. EPA national inventory (available from U.S. EPA, Office of Air Quality Planning and Standards, Research Triangle Park, NC, 27711). The resulting pattern was then divided by the total CO emitted during 24 hours. This gave a normalized, mass-conserving function that was used to weight emissions as a function of local time. These area sources include managed and wild forest fires, agricultural burning, commercial, agricultural, industrial, and recreation equipment, off-highway vehicles (including aviation, railroads, and marine vessels), and the burning of wood, oil, coal, and natural gas. Figure 2 shows the resulting temporal

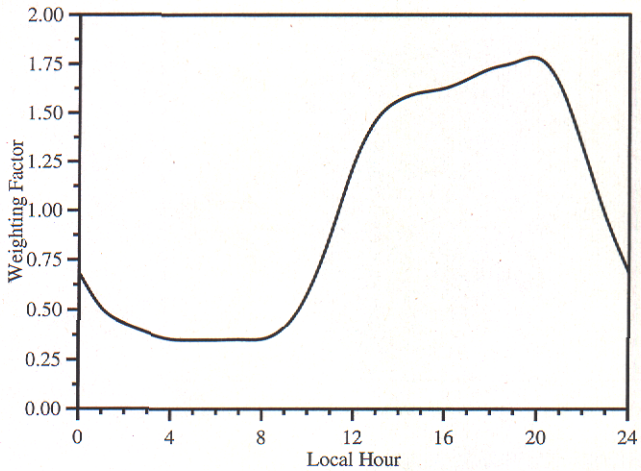

Figure 2. The diurnal variation weighting function applied to model CO emissions for CASE3.

variation in emissions. This function is not expected to be representative throughout the model domain. It was chosen to provide a reasonable pattern (perhaps more realistic than a simple step function or sine wave) to apply to the entire domain and examine potential effects of adding diurnally varying emissions to the model.

3.2. Vertical Weighting Technique

To compare the MAPS observations with simulated mixing ratios, we used a method developed by *Reichle et al.* [this issue] and *Pougatchev and Sachse* [1997] to vertically integrate and weight the model data. Briefly, the method involves summing the product of the number of molecules in a layer, the modeled CO mixing ratio interpolated to that layer, and the MAPS averaging kernel for that layer. The sum is then divided by the total number of molecules in the atmospheric column. The MAPS averaging kernel is a function that is used to relate measured CO column amount to the vertical profile of CO mixing ratios. The kernel was computed for a 40-layer U.S. standard atmosphere with a uniform CO mixing ratio of 110 ppbv. Because we only compared relative magnitudes (for reasons described below), we truncated this summation at the highest model level. This resulted in a bias of about +6.1 ppbv in the simulated column-averaged CO mixing ratios. The vertically weighted integration was performed for all times and all data points and then temporally averaged as desired.

4. Brief Summary of Observed Meteorology

During the MAPS mission the meteorology of the western portion of the model domain was dominated by the eastward progression of three frontal systems. Rainfall was associated with each of these fronts, which passed over the U.S. east coast on April 10, 13, and 16 before moving over the western Atlantic. Two systems passed over the European portion of the domain during this time period: one during April 9 through 13, and another from April 15 through 18. Figure 3 shows 850 and 500 hPa streamlines averaged over the MAPS mission time period. At the 850 hPa level the flow is dominated by anticyclonic motion centered in two regions of the North Atlantic and cyclonic motion in central Europe and northern Canada. At the 500 hPa level there is anticyclonic motion over the northeastern Atlantic and the Caribbean Sea and cyclonic motion in central Europe, with a strong westerly pattern elsewhere. A more detailed account of synoptic weather during the April 1994 MAPS mission is given by *Faluvegi* [1997].

5. Results and Discussion

5.1. Comparisons of Observed and Simulated Meteorology

We examined several meteorological fields for various geographic locations, altitudes, and times. In particular, horizontal and vertical winds and convective rainfall were examined most closely, as these are important to transport. (The spatial extent of convective rainfall indicates regions of subgrid-scale vertical motions, which are important for vertical transport of a passive tracer.) There is good agreement between these simulated fields and meteorological observations from the National Weather Service (NWS) and the European Centre for Medium-Range Weather Forecasting (ECMWF).

Figure 4 depicts model vertical velocity for 1200 UTC April 13 (Figure 4a) and 1200 UTC April 14 (Figure 4b) for model layer 11 (near 500 hPa). Superimposed in black are the locations of observed surface fronts and low-pressure centers. As the fronts move from the eastern U.S. coast out to sea during these 24 hours, the model vertical motions move accordingly, with upward motion in advance of the cold front and over the warm front and low, and subsidence behind the cold front and to the southwest of the low. Figure 5 shows observed (Figure 5a) and simulated (Figure 5b) regions of daily averaged precipitation for April 13. The two plots indicate similar patterns in rainfall, consistent with meteorological analyses from the NWS and the National Centers for Environmental Prediction (NCEP)/NCAR Climate Data Assimilation System (CDAS) reanalysis project.

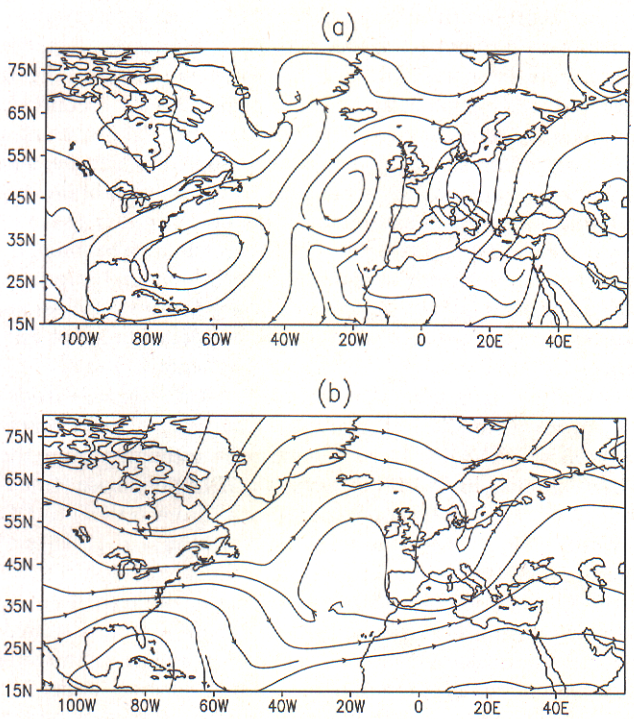

Figure 3. The (a) 850 hPa and (b) 500 hPa streamlines averaged over the MAPS mission time period derived from ECMWF winds.

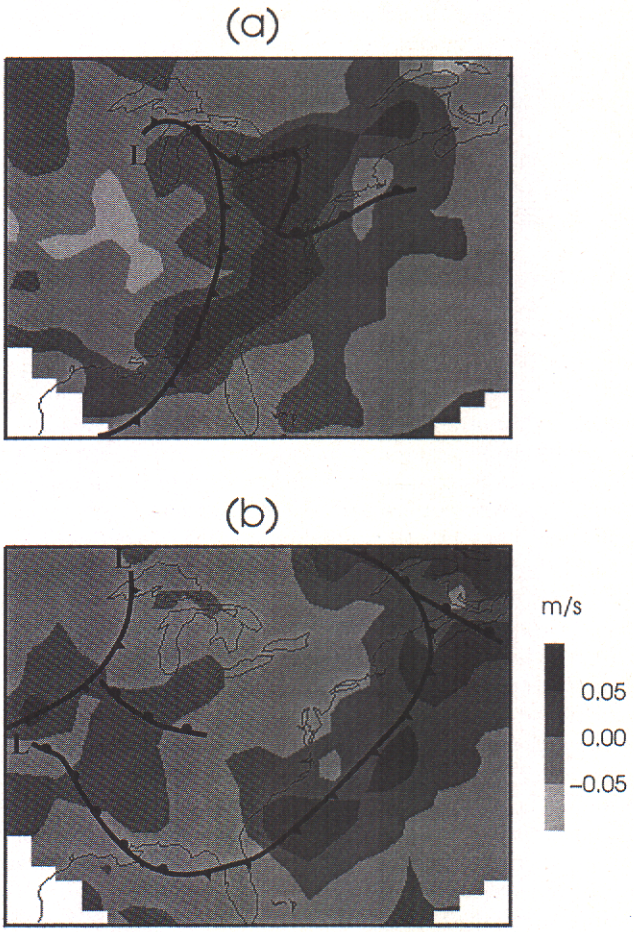

Figure 4. Simulated vertical velocity for (a) 1200 UTC April 13 and (b) 1200 UTC April 14 for model layer 11 (near 500 hPa). The locations of observed surface frontal systems and low-pressure centers are superimposed in black.

5.2. CASE1: Control Simulation

5.2.1. Simulated CO mixing ratios. In the lower model layers, CO mixing ratios are influenced by the distribution of sources, vertical mixing in the PBL, and horizontal transport. Figures 6a and 6b show horizontal cross sections of simulated CO mixing ratios in the lowest model layer over Europe for 0500 UTC and 1300 UTC April 12. For a constant CO emission rate these figures illustrate the typical diurnal variation in simulated mixing ratios in the lower layers. During local night, CO is trapped in the stable nocturnal PBL, and mixing ratios increase. In less stable daytime conditions, CO mixes vertically with the growing PBL, and low-level mixing ratios decrease. For example, over the region of maximum emissions (see Figure 1), CO mixing ratios decrease from about 375 ppbv at 0500 UTC to about 225 ppbv by 1300 UTC. In addition to this diurnal variation in mixing ratios due to vertical mixing, the simulated CO also slowly spreads horizontally with the low-level winds.

As expected, the influence of the PBL grows weaker with altitude. Above the PBL the simulated CO behaves like plumes, rising to the upper levels and then spreading horizontally with the comparatively strong winds. We compared horizontal cross sections of CO for model layer 11 (near 500 hPa) with observed meteorology from the NWS, the ECMWF, and the NCEP/NCAR CDAS reanalysis project. These comparisons indicate that the motions of fronts and lows are mirrored as increasing mixing ratios in upper levels. Likewise, the presence of high pressure in a region confines CO to lower levels. In general, the simulated horizontal transport of CO is consistent with observed 500-hPa winds.

As an example of such comparisons, Figure 7 shows a cross section of simulated CO mixing ratios for 1200 UTC April 16, near 500 hPa. Superimposed in black are the locations of observed surface fronts and low-pressure centers. The effects of the low and the synoptic fronts can be seen as high-CO

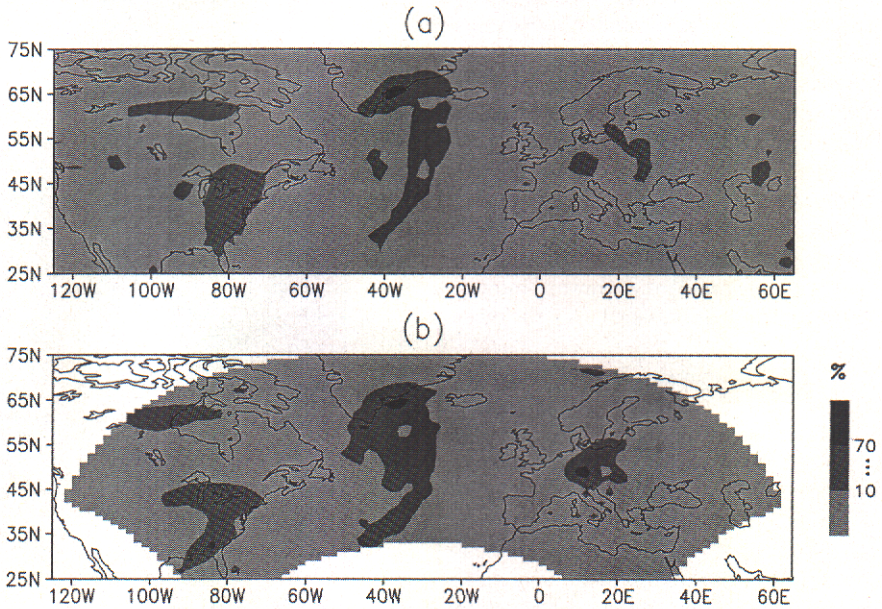

Figure 5. (a) Daily average observed regions of precipitation for April 13 from the NCEP/NCAR CDAS reanalysis project and (b) coincident simulated rainfall regions. Both plots have been normalized to their maximum values.

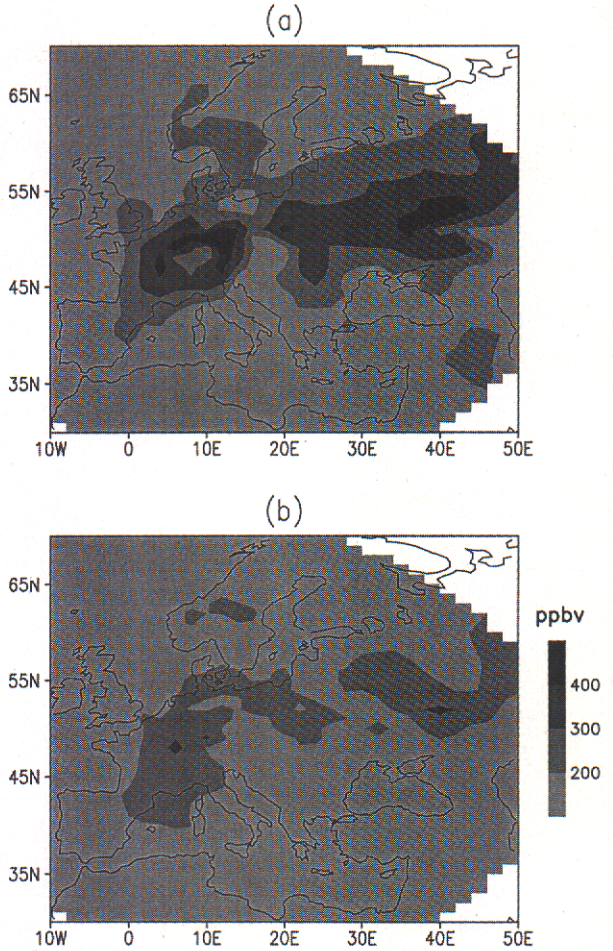

Figure 6. Horizontal cross sections of simulated CO mixing ratios in the lowest model layer over Europe for (a) 0500 UTC April 12 and (b) 1300 UTC April 12.

regions in the figure. The CO spreads with the cyclonic winds around the low, consistent with 500-hPa wind observations (not shown).

In our simulations, regions of high CO mixing ratios in upper levels moved horizontally with the motion of frontal systems. We found upward transport in advance of the fronts and subsidence behind. *Wang et al.* [1996] used MM5 (with a higher-resolution nested grid but a smaller domain) to simulate CO transport as a passive tracer during a midlatitude squall line event. That study also found that enhanced upper tropospheric CO propagated with the squall line and that downward motion behind the squall line transported upper-level CO to lower levels.

Figure 8 shows profiles of changes in simulated CO mixing ratios due to cloud transport, vertical and horizontal advection, and vertical diffusion averaged over the MAPS mission and midlatitude land grid cells. In the lowest 0.5 km, vertical diffusion (due to PBL mixing) and upward transport by clouds contribute most strongly to changing CO mixing ratios. From about 0.5 to about 3 km, all four processes contribute comparably. Above about 6 km, transport is dominated by advection.

5.2.2. Comparisons with MAPS data. As described in section 3.2, a weighted vertical integration was performed on the model CO data in order to compare them directly with MAPS data. Figure 9a shows the MAPS 5° × 5° interpolated, mission-averaged CO observations. Figure 9b shows the vertically integrated model data averaged over the 10 days of the MAPS mission. The spread in the model data is about 38 ppbv, while the spread in the MAPS data from this domain is about 60 ppbv. Therefore the model predicts that the prescribed surface emissions could have a significant impact on MAPS-like observations on a weekly timescale. However, the fact that the spread in model data is significantly smaller than the spread in observations suggests that there are other factors, which have not been modeled, influencing the MAPS observations. Some possible influencing factors are presented later in this section. Because of this difference in range of CO mixing ratios, we make qualitative comparisons here.

Both the observations and model simulation show highest values over northeastern Europe, near the Baltic Sea, with lower values over southern and western Europe. Model predictions and observations are both low over North Africa. Over North America, both model and observations show a maximum near the southeastern Hudson Bay. However, the model predicts higher values extending toward the mid-Atlantic U.S. coast. The model fails to reproduce regions of high CO west of the central United States due to the lack of model emissions from the U.S. West Coast and beyond. Over the ocean, both figures generally depict highest values over northern regions and off the east coast of Canada and west coast of Ireland. In general, the model underpredicts the magnitude of CO mixing ratios over the Atlantic, north of 30°N. However, plots with additional contours (not shown) accentuate similar qualitative features, such as the region of relatively low CO mixing ratios centered around 35°W and stretching from the southern edge of the domain northward.

In general, the best agreement occurs over land in Europe. This is not surprising, since this region is strongly influenced by local sources and the least influenced by the lack of emissions information propagating from the extreme west of the domain. The largest discrepancies are the higher model CO over the northeastern United States and lower CO over the parts of the Atlantic.

On shorter timescales, MAPS observations are limited to

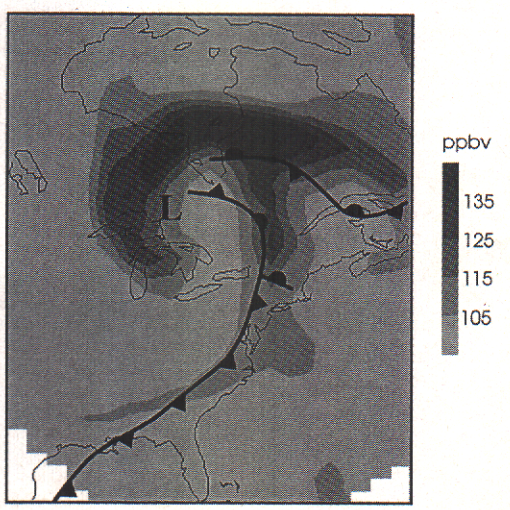

Figure 7. Cross section of model layer 11 (near 500 hPa) simulated CO mixing ratios over the eastern United States for 1200 UTC April 16. The locations of observed surface frontal systems and low-pressure centers are superimposed in black.

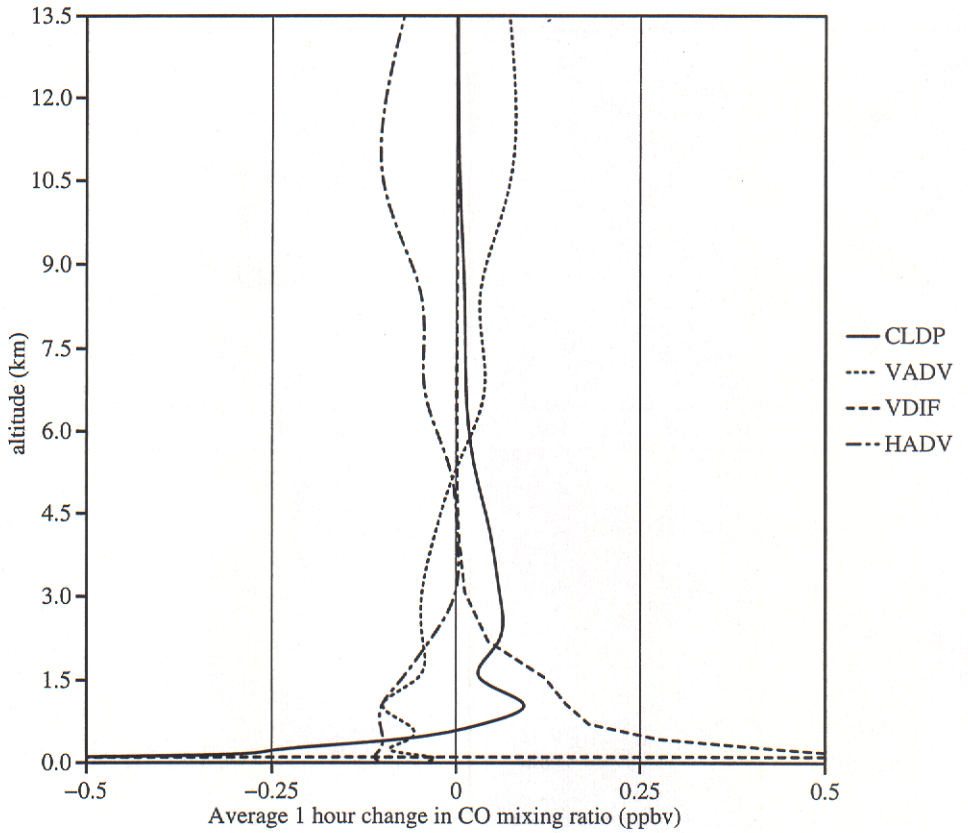

Figure 8. Profiles of the contributions of cloud transport (CLDP), vertical advection (VADV), vertical diffusion (VDIF), and horizontal advection (HADV) to changing CO mixing ratios. Profiles are averaged over the MAPS mission time period and midlatitude land grid cells.

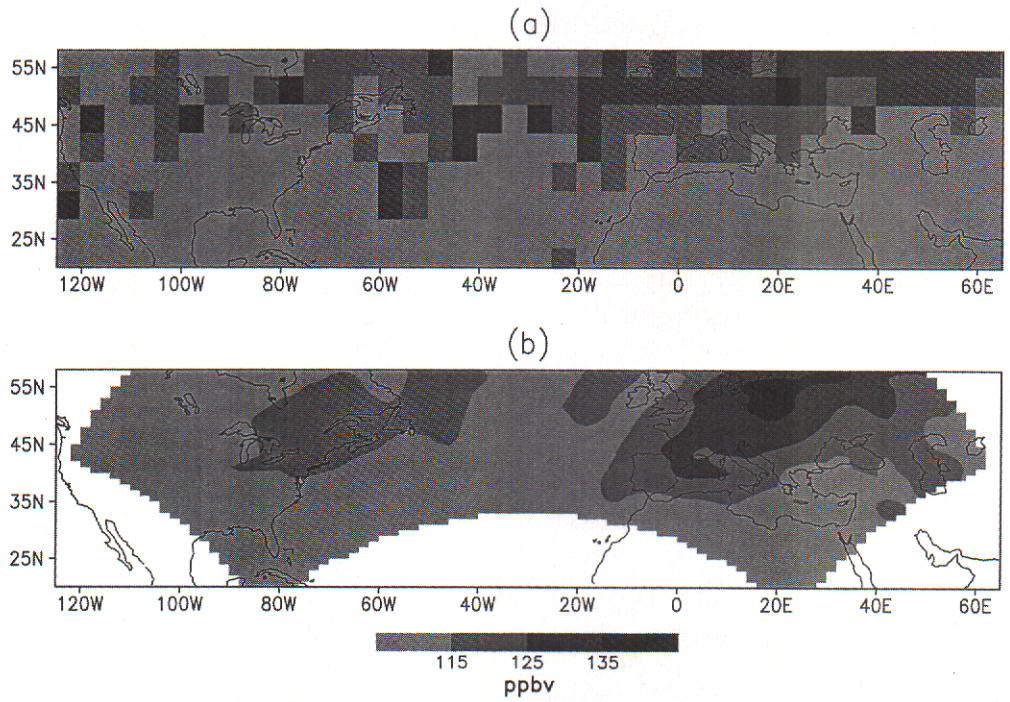

Figure 9. (a) MAPS 5° × 5° interpolated mission-averaged CO mixing ratios. (b) Vertically weighted and integrated simulated CO mixing ratios averaged over the 10 days of the MAPS mission.

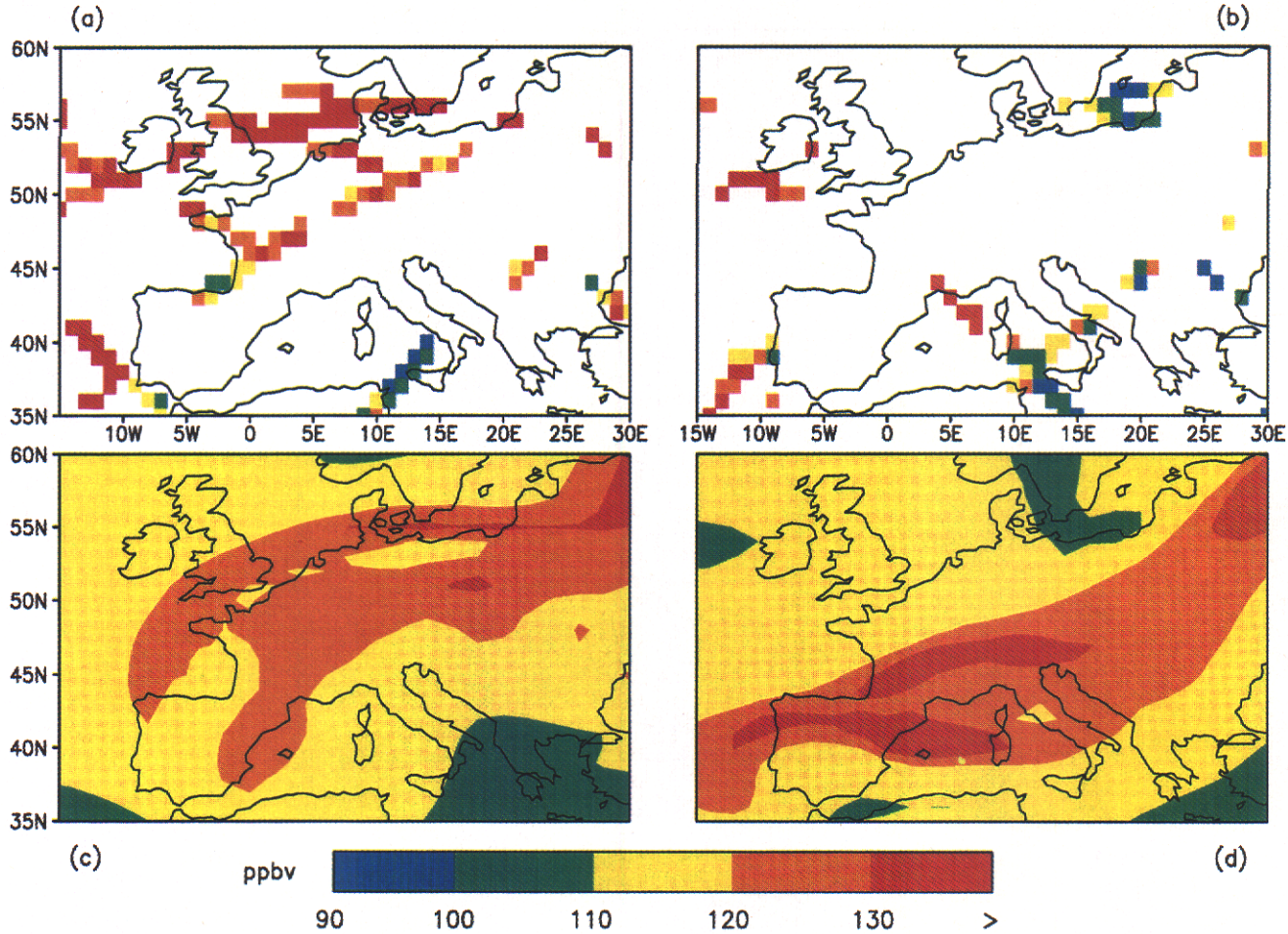

Plate 1. MAPS CO mixing ratios over Europe for (a) April 16 and (b) April 18, and simulated CO mixing ratios over Europe for (c) April 16 and (d) April 18.

cloud-free regions over the space shuttle's ground track. Therefore it is important not to generalize these observations over large geographic regions. Plate 1 compares European MAPS data (Plates 1a and 1b) and model data (Plates 1c and 1d) for April 16 and April 18. In the vicinity of northern Germany and Poland and the Baltic Sea, CO values remain high in both observed and modeled data during most of the MAPS mission time period. However, both MAPS and model data show a drop in CO over this region between April 17 and 18, associated with regional changes in wind patterns.

Plate 2 depicts MAPS CO mixing ratios for April 11 and April 11 daily averaged simulated CO mixing ratios. On this day, MAPS observed high CO where the space shuttle passed over northern Europe, which is consistent with model predictions, and both model and observations indicate that this region of high CO had spread toward the southwest since April 10 (not shown). In addition, the model simulates the observed increase of CO in the western Atlantic, which is the result of transport from the U.S. east coast by the offshore movement of a frontal system. The contrast between relatively low values in the eastern Atlantic and higher values in the west are evident in both model data and available observations.

There are several potential sources of discrepancy between simulated and observed CO. Most fundamentally, the simulated mixing ratios are not the equivalent of MAPS observations. Instead, model data represent the distribution of predicted contributions to the MAPS mixing ratios due to the prescribed model surface emissions. Clearly, other components exist in the MAPS observations. For example, the omission of a methane oxidation CO source and the significant uncertainty in included source components were already addressed in section 3.1. In addition, simplified initial conditions and boundary conditions may cause the model to underestimate the range of CO mixing ratios. Since the model simulation began with a uniform background mixing ratio on March 30, no information on emissions or transport prior to that date is contained in the simulated CO mixing ratios. The specified constant inflow boundary condition can also contribute to discrepancy. For example, CO-enriched air originating from southern California and advecting across the western domain boundary is not modeled.

At least three general characteristics of the comparisons made above suggest that simplifications in initial conditions may contribute to discrepancies: (1) Most of the discrepancy in the range of CO mixing ratios between simulations and observations occur below 100 ppbv. The uniform 100 ppbv used as both initial conditions and inflow boundary conditions biases the model against these lower mixing ratios. (2) The fact that comparisons between the simulations and observations are best in regions of strong emissions and worst over the remote Atlantic point to the lack of above-background CO transported over the ocean prior to early April. (3) The fact that qualitative

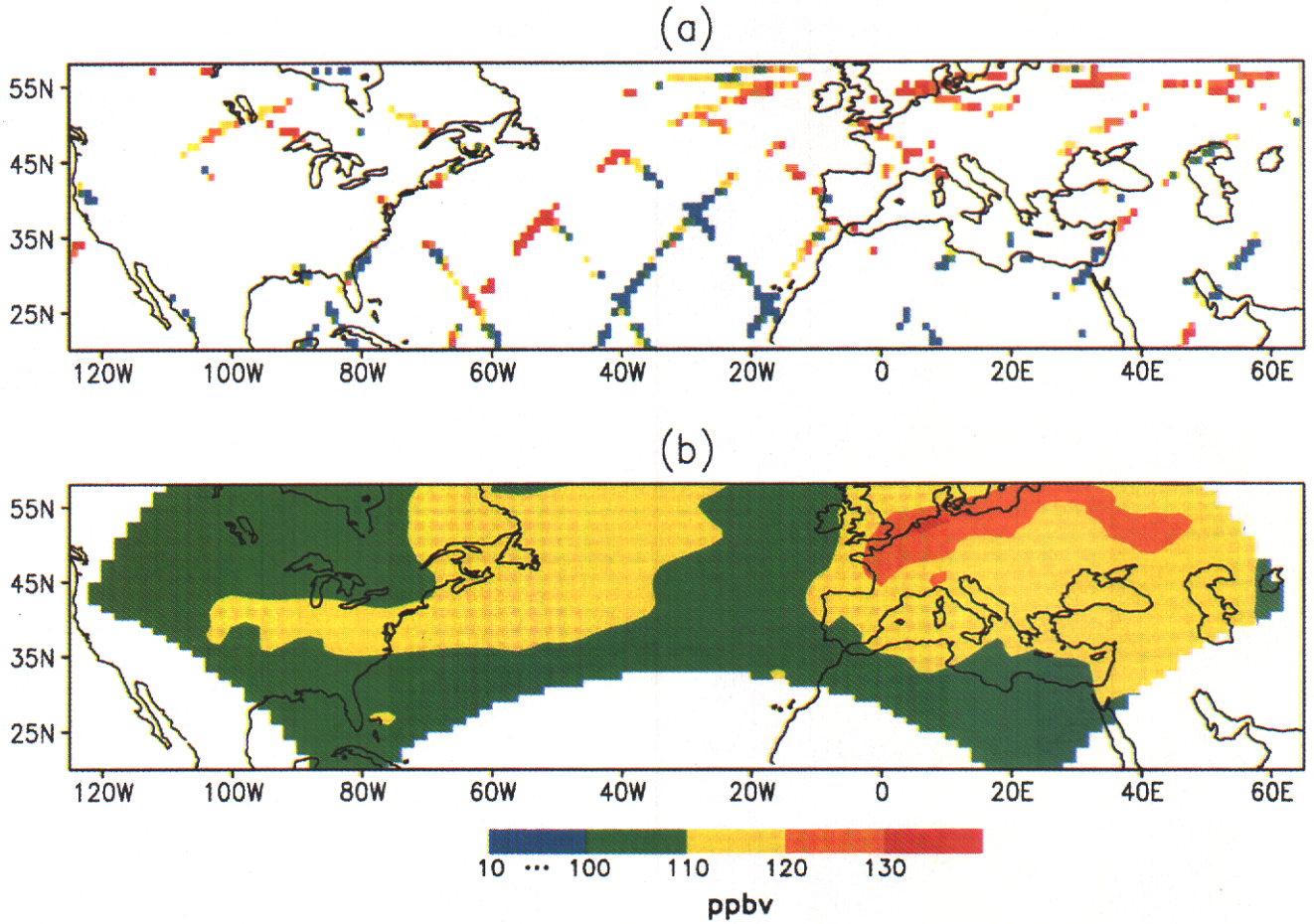

Plate 2. (a) MAPS and (b) simulated CO mixing ratios for April 11.

comparisons of the spatial and temporal distribution of CO fare better than direct quantitative comparisons suggests that simplified initial conditions and uncertainties in CO source magnitudes are more important than unrealistic transport.

It is difficult to quantify the uncertainty caused by these simplifications. However, one clue is provided by comparison with a model simulation which started with uniform initial conditions on April 9 rather than March 30 (not shown). From this comparison we found that improving the April 9 initial conditions by using the March 30 to April 9 simulation increased the range of simulated mission-averaged CO mixing ratios by roughly 83% (almost entirely by increasing the maximum value). However, by the end of the March 30 to April 19 simulation the CO within the domain approaches a steady state, as advection out of the domain begins to balance the CO emissions. Therefore extending the simulation time prior to March 30 would not proportionally increase the range in simulated CO mixing ratios.

Another possible reason for differences between model and MAPS data involves the discarding of cloud-contaminated CO data from the MAPS data set. Strong vertical motion, which lifts CO to MAPS-sensitive levels, often causes cloudiness as well. MAPS does not measure high CO mixing ratios under these conditions (R. Newell, Atmospheric processes influencing measured carbon monoxide in NASA Measurement of Air Pollution From Satellites (MAPS), submitted to *Journal of Geophysical Research*, 1998). For example, the three strongest contributions to high modeled CO mixing ratios in upper levels over the east coast of the United States occurred due to upward transport of CO on April 10, 13, and 16. The MAPS daily plots show that very few useful CO data were obtained over land in the northeastern United States on those days, due to cloudy conditions.

Plate 3a shows MAPS observations for April 10 over the northeastern United States. Plate 3b shows the vertically integrated model data for 1900 UTC April 10 for the same region. (MAPS orbit plots indicate that the observations over the Great Lakes were taken around 1900 UTC.) Plate 3c depicts the average observed cloudiness for the same day. These figures illustrate the model suggestion that the MAPS measurements over the Great Lakes region were taken over an area of relatively low CO mixing ratios between two higher-CO regions to the north and south of the Great Lakes. The space shuttle ground track also passed over the region of higher model CO over the U.S. east coast, where no MAPS data are available due to clouds. Finally, over the ocean (near 37°N, 72°W), MAPS picks up higher CO than over the Great Lakes. This pattern is consistent with model predictions.

This cloud effect is not as pronounced over northern Europe because stronger emissions and less persistent westerly flow maintain high CO mixing ratios over northern Europe during most of the MAPS time period. On the other hand, the model suggests greater variation over the eastern United States. Consequently, the MAPS instrument may have had more opportunity to measure high CO values over Europe. In addition, northern Europe is at a higher latitude than the region of

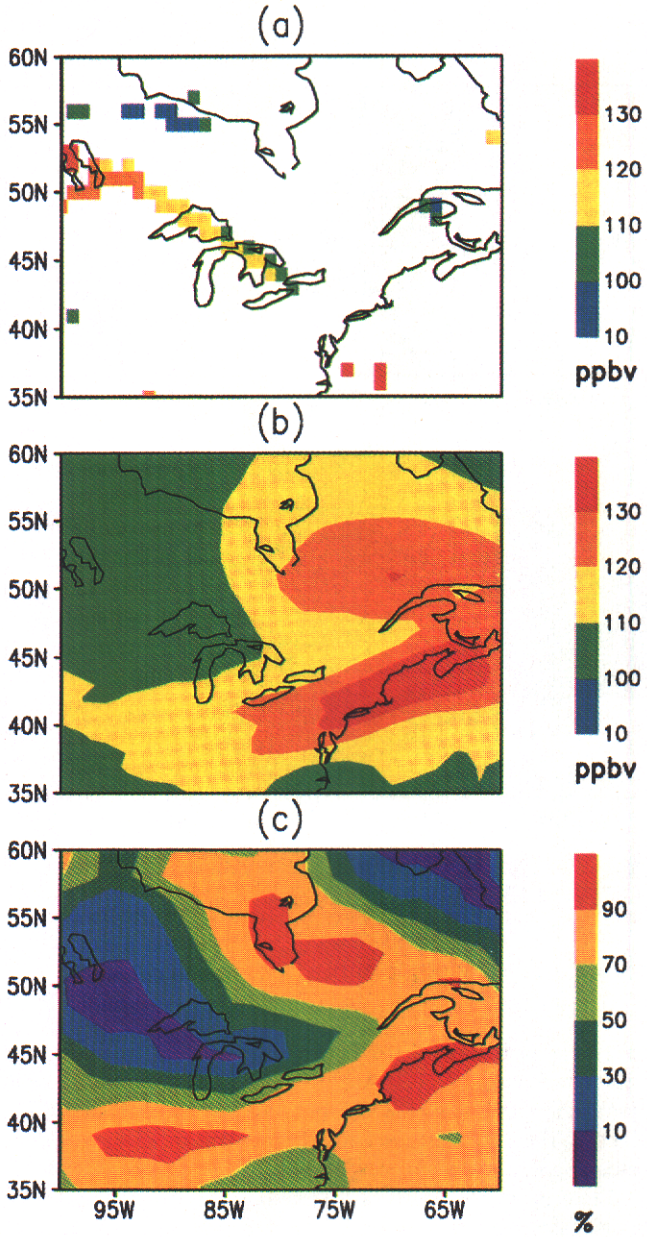

Plate 3. (a) MAPS CO mixing ratios for April 10 over the northeastern United States. (b) Vertically weighted and integrated simulated CO mixing ratios for 1900 UTC April 10. (c) Average observed cloudiness (%) for April 10 from the NCEP/NCAR CDAS reanalysis project. MAPS orbit plots (not shown) indicate that April 10 CO observations over the Great Lakes were made around 1900 UTC.

maximum North American emissions, and is therefore sampled more frequently by the MAPS instrument, due to the space shuttle ground track.

5.3. CASE2: Effects of Cumulus Convection

To study the effects of subgrid-scale cloud transport on CO distributions, we turned off the cloud scheme and performed a new simulation (CASE2) for the same time period as CASE1. All other model conditions remained the same. Simulated mixing ratios were averaged over the MAPS mission time period and over the horizontal domain for each model layer. The resulting average profile is shown in Figure 10, along with the same profile for CASE1, the difference of these two profiles, and the MAPS averaging kernel. This figure shows that the average effect of removing cloud transport is an accumulation of CO in the lower model layers and a corresponding deficiency in upper layers. Since the averaging kernel is strongest in the middle to upper troposphere and weakest near the surface, a weighted vertical integration for an average grid cell produces a small decrease ($\approx -0.25\%$) in CO mixing ratio when vertical cloud transport is removed. Similar temporally averaged difference profiles (not shown) calculated for large portions of the United States, Europe, and the Atlantic also point to greater mixing ratios in the lowest few kilometers and less CO in upper layers. However, the upper-level depletion is strongest over Europe, and the low-level increase is significantly smaller over the ocean, due to weaker emissions.

Figure 11 shows the difference in the mission-averaged, vertically weighted and integrated mixing ratios between CASE2 and CASE1. In general, the difference is positive over much of the eastern United States and North Atlantic and in isolated regions of Europe. There is generally a weak negative difference elsewhere, with regions of stronger negative differences over Europe. The figure illustrates that the average negative effect on the MAPS-like mixing ratio is not the result of a small negative value everywhere, but of the average of a complicated pattern of negative and positive regions. The reason for this complexity is that not all "difference profiles" are the same. Instead, they vary with the duration and strength of the convective cloud events and local emissions and according to the history of all previous transport at the particular grid square. Consequently, upon vertically weighting and integrating the profiles, some grid cells have a net negative effect (much like the average case in Figure 10), but some have a net positive effect, with higher low-level values but less depletion of upper-level CO. In more remote and relatively cloud-free regions, difference profiles are often slightly negative throughout most of the model atmosphere.

Figure 12 provides an example of cloud effects. It depicts the difference (CASE2 − CASE1) in CO mixing ratios for model layer 11 (~5400 m, Figure 12a) and model layer 1 (~38 m, Figure 12b) for 1200 UTC April 13. The meteorological situation at this time was described in section 5.1 and Figure 4a. Figure 12 shows that the lack of convection causes an abundance of CO in the lowest model layer. This effect is particularly strong over land, where CO sources and convection are strongest. At upper levels there is less CO in CASE2 than CASE1 over the warm front, in advance of the cold front, and spreading out over the Atlantic. Figure 13 presents difference profiles for selected locations and times. Curve 1 in Figure 13 is a difference profile for a grid cell in the vicinity of this cold front. As expected, it depicts more CO in lower levels and less in upper levels in CASE2, and results in a net negative effect.

However, a competing mechanism keeps the average vertically integrated effect of removing cloud transport small. Because the lack of cloud convection resulted in higher CO mixing ratios in low model layers after the frontal systems passed through the region, there was more CO available for transport by vertical advection as low pressure moved into the region. This explains the higher CO in the upper levels in the vicinity of the low-pressure center in CASE2. A difference profile for a grid cell near this low is depicted in curve 2 of Figure 13, which shows increased CO in both the boundary layer and

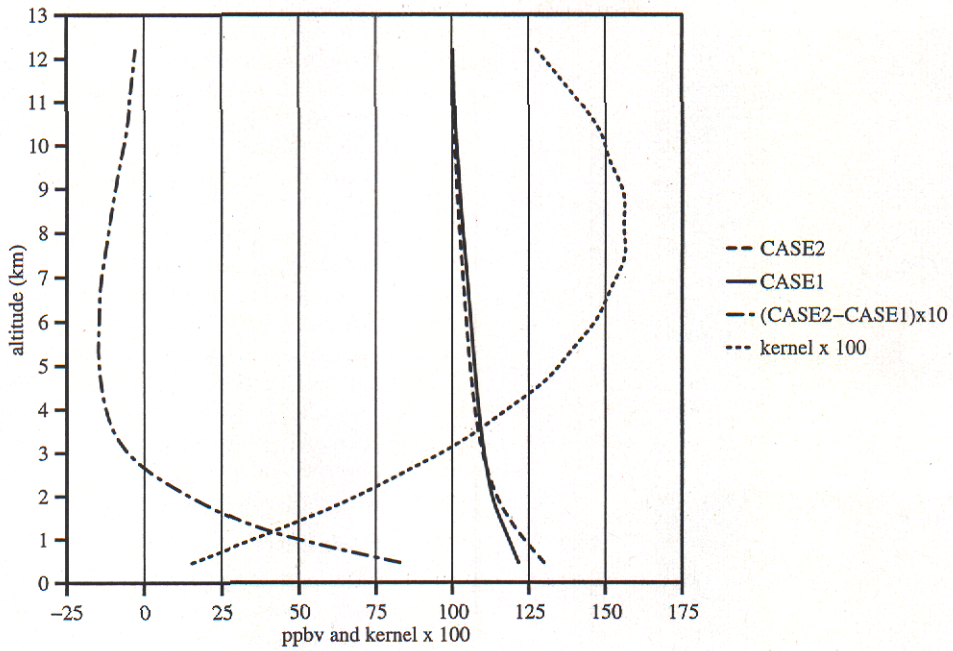

Figure 10. Profiles of the CASE1 and CASE2 simulated CO mixing ratios averaged over the MAPS mission and the horizontal domain. Also shown are the MAPS averaging kernel (multiplied by 100 to preserve the scale of the plot) and the difference in the two profiles (CASE2 − CASE1) (multiplied by 10 to preserve the scale of the plot).

much of the free troposphere, resulting in a net positive effect for that grid cell.

The mission-averaged pattern from Figure 11 can be explained in terms of three-dimensional atmospheric motions and the MAPS averaging kernel. For example, the following is a sequence of events that can lead to the strong gradient pattern modeled over Europe. Since model CO emissions are strongest in northern central Europe, the CASE2 increases in boundary layer CO are strong there. There is a corresponding depletion in upper layers in this region, but comparatively strong upper-level winds transport the relatively clean air away and diminish this local negative effect above the strong source region. This horizontal advection (combined with the effects of vertical advection near a low described above) may be strong enough to leave a local net positive effect upon vertical integration. Also, as CASE2 advects relatively clean air away from the region, it spreads the upper-level negative effect over other parts of Europe and the ocean, where emissions are weaker. A difference profile in such a region is given in curve 3 of Figure 13, which shows strong depletions of CO in the free atmosphere, resulting in a net negative effect upon vertical integration.

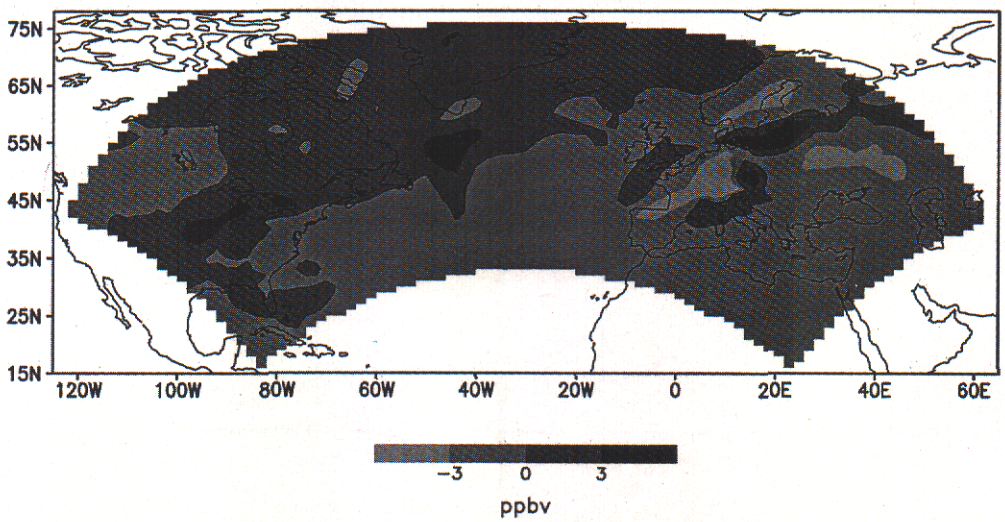

Figure 11. CASE2 − CASE1 mission-averaged, vertically weighted and integrated simulated CO mixing ratios.

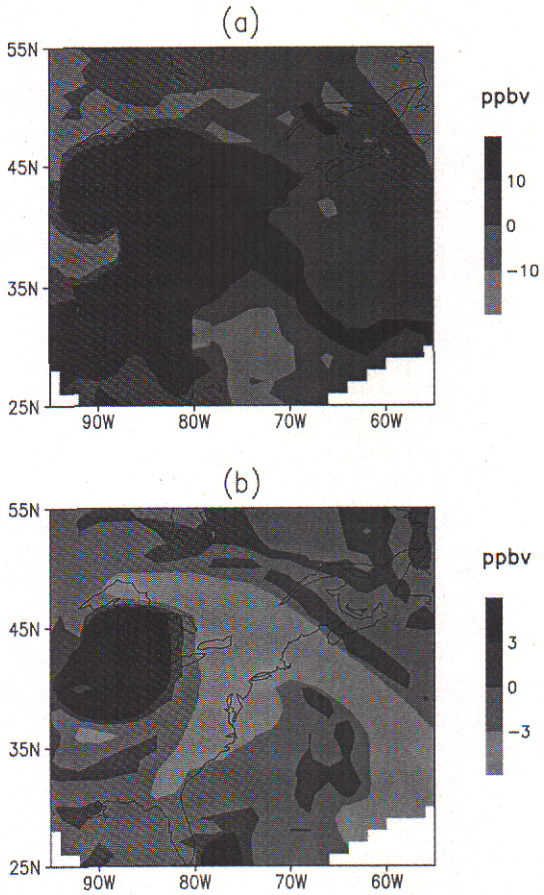

Figure 12. CASE2 − CASE1 simulated CO mixing ratios for 1200 UTC April 13 for (a) model layer 11 (~5400 m) and (b) model layer 1 (~38 m).

The CASE2 results confirm that cumulus convection is an important mechanism for transporting CO to the free troposphere. *Wang et al.* [1996] also found that subgrid-scale transport was a major component of the total upward CO transport. The instantaneous and local effects of clouds are much stronger than the large-scale average case suggests. *Lin et al.* [1996] also draw this conclusion by studying the transport of ^{222}Rn over the eastern United States and the western North Atlantic. They found a vertical redistribution pattern similar to that of the current study. However, the redistribution pattern in the Lin et al. case was significantly stronger, since that study simulated August conditions, which are generally more convective for the eastern U.S. domain.

While the average effects of removing cloud transport may be intuitive, clearly it is not the result of a simple, linear process. Instead, the MAPS averaging kernel interacts with several physical and dynamical processes that compete and cooperate to determine the vertically integrated result.

5.4. CASE3: Effects of Diurnal Emission Variations

In CASE1 and CASE2, CO was emitted at a constant rate. We performed an additional simulation that included a diurnal variation in emissions (CASE3). The temporal variation in emissions is described in section 3.1. Simulated CO mixing ratios from CASE1 are subtracted from CASE3 mixing ratios in order to clarify differences.

As expected, the differenced (CASE3 − CASE1) mixing ratios in the lowest model layers closely follow the emissions variation; local mixing ratios in the PBL are higher when CO emissions exceed the constant CASE1 value and lower when less CO is emitted. The impact is strongest in regions of high total emissions. After a short lag, this alternating pattern of enhanced and depleted CO is detectable at upper levels in the form of alternating plumes of positive and negative difference

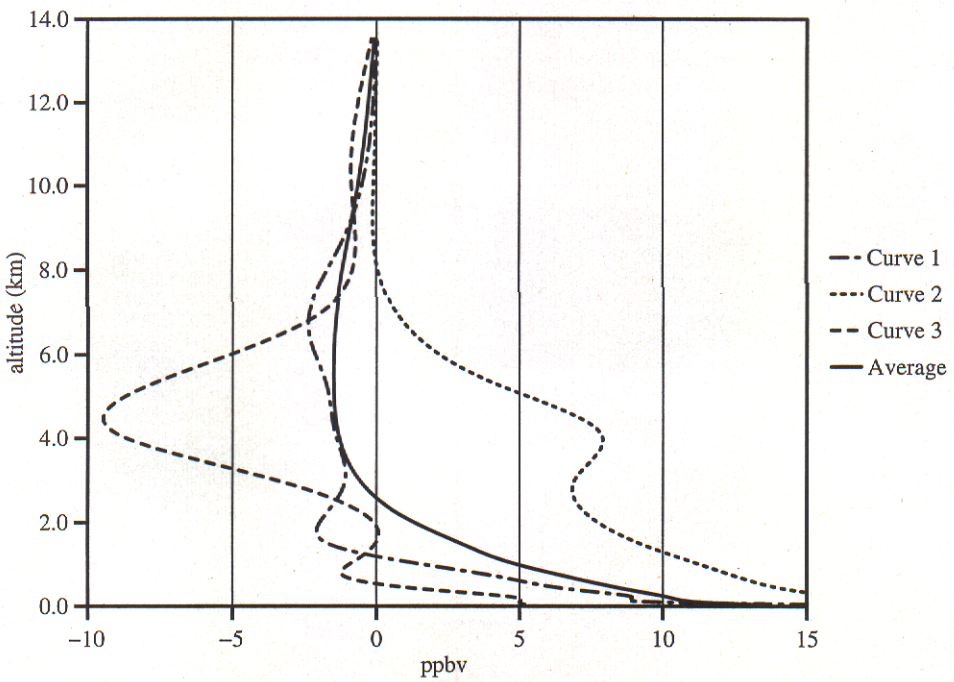

Figure 13. Profiles of CASE2 − CASE1 simulated CO mixing ratios for a grid cell near a frontal system (curve 1), a grid cell near a low-pressure center (curve 2), a grid cell downwind of a region of strong convection and CO surface emissions (curve 3), and a horizontal and temporal average of all grid cells (average).

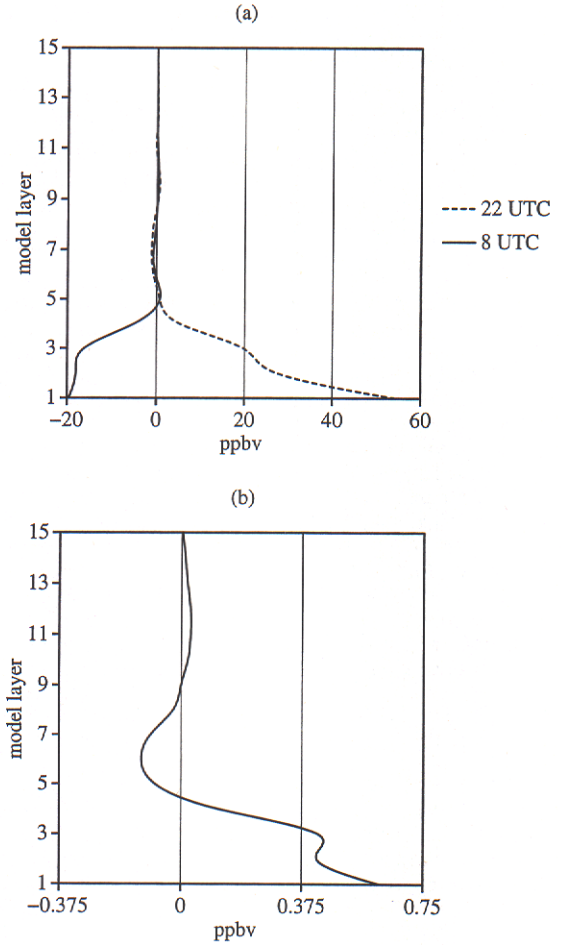

Figure 14. (a) Profiles of CASE3 − CASE1 simulated CO mixing ratios for 0800 UTC and 2200 UTC (average of 5 days of 0800 and 2200 UTC simulated mixing ratios) for a grid cell in northern central Europe (near 53°N, 17°E). (b) Profile of CASE3 − CASE1 simulated CO mixing ratios averaged over the MAPS mission and the horizontal domain. Note the difference in mixing ratio scale between Figures 14a and 14b.

values. Figure 14a shows difference profiles for 0800 UTC and 2200 UTC (average of 5 days of 0800 and 2200 UTC simulated mixing ratios) for a grid cell in northern central Europe (near 53°N, 17°E). These two times of day were chosen to maximize the difference in prescribed CO emissions, while keeping the difference in PBL dynamics small. The two profiles show differences of opposite sign in the lower model layers. For this grid cell the lowest-layer differences are roughly −20 to +50 ppbv, but differences of over ±100 ppbv on particular days are not uncommon. The differences are much smaller in upper levels.

These diurnally alternating positive and negative effects limit the magnitude of the time-averaged effect for any given layer. Figure 14b shows the horizontally and temporally averaged vertical difference profile for CASE3 − CASE1. Note that the space- and time-averaged differences are significantly smaller than differences for a specific region and time (compare the ranges of mixing ratios between Figures 14a and 14b).

Despite this small average effect, we can suggest some factors that influence the shape of this profile (Figure 14b). In the lower model layers, horizontally averaged CO difference profiles oscillate diurnally between a positive and negative effect. However, when temporally averaged, the positive effect slightly outweighs the negative, due to asymmetry in the temporal distribution of emissions (Figure 2) and diurnal changes in the PBL height.

Above the PBL the profile is influenced by convective clouds. The cumulus convection transports CO from lower to upper levels, whether the mixing ratios are enhanced or depleted by the diurnal emissions. However, since convection is more efficient under more unstable daytime conditions, the vertical transport of enhanced mixing ratios is favored over that of depleted mixing ratios. This results in a net increase in CO mixing ratios above about 3 km (around model layer 9), and a decrease below, contributing to the negative segment of the profile from about 0.5 to 3.0 km (around model layers 4 through 8).

The vertically integrated and MAPS mission-averaged CASE3 CO mixing ratios (not shown) indicate very little change compared to CASE1, the simulation with a constant emissions rate. There are no changes greater than ±0.5 ppbv, and the change for an average grid cell is $\lesssim$+0.01%. Therefore, while significant changes occur for individual locations and times, a diurnal variation in CO emissions did not significantly improve or degrade comparisons with MAPS observations on the mission-averaged timescale.

6. Conclusions

CO transport during the April 1994 MAPS mission was simulated using a chemistry and transport model (MAQSIP) driven by a meteorological model (MM5) that utilizes assimilated meteorology. Synoptic features and associated rainfall extent were found to be well simulated by MM5.

Simulated CO mixing ratios were explained in terms of PBL diurnal variations, synoptic-scale motions, convection, and surface emissions distribution. The fact that modeled CO distributions are strongly influenced by prevailing meteorological features is compelling evidence that fronts and low-pressure systems are important processes for transporting CO to upper levels.

Qualitative comparisons with MAPS data agree in several locations and on several timescales. However, the model predicts higher values over the northeastern United States and lower values over much of the Atlantic. We found a spread in the magnitudes of mission-averaged model CO mixing ratios of approximately 38 ppbv, while the corresponding spread in MAPS observations is approximately 60 ppbv. This suggests that CO surface emissions have a significant effect on MAPS observations on a weekly timescale. However, the fact that the range in simulated CO mixing ratios does not cover the full range of observed mixing ratios suggests significant effects from components that were not modeled. Some likely sources of discrepancy include the following: the simplified initial conditions and boundary conditions (see section 5.2.2), the neglected methane oxidation source and uncertainties in CO emissions (see section 3.1), and the fact that the MAPS instrument could miss high CO measurements due to abundant cloud cover (see section 5.2.2).

A simulation performed with the cumulus convection scheme turned off had an average effect of increasing mixing ratios in the lower model layers and depleting CO above. The simulation suggests that the mission-averaged effect on the MAPS mixing ratios due to the absence of cloud transport

would be a complex pattern of increases and decreases, due to several competing mechanisms, but that the mixing ratio for an average grid cell would decrease slightly ($\approx -0.25\%$). Despite this small effect on the large-scale average, instantaneous local effects of clouds on CO distributions are significant.

A simulation that included a diurnal variation in CO emissions produced significant changes in mixing ratios for a given time and location that were consistent with the prescribed diurnal pattern in emissions. However, the mission-averaged effects on the MAPS-like mixing ratios were minimal ($\lesssim +0.01\%$ for an average grid cell).

Further research could examine the effects of including a methane oxidation source, improving lateral CO boundary conditions, and further refining the diurnal emissions pattern. A longer simulation time prior to the MAPS mission time period could also be used to improve the initial CO mixing ratio field, as long as the passive tracer assumption remains valid. Many other potential improvements may not be warranted without a better estimate of initial (background) CO distributions.

Acknowledgments. This research was supported in part by NASA Langley Research Center grant NAG-1-1752 and the State Climate Office of North Carolina. R. Mathur acknowledges partial support through NASA grant NAGW-4701. We would like to thank S. Nolf (NASA LaRC) for assistance with MAPS data, J.-F. Müller (IAS) for assistance with CO emissions data, and T. Odman, S. Thorpe, and M. Houyoux (MCNC) for support regarding models, data visualization, and EPA CO emissions data. CO emissions data are from NCAR/IAS, and NMHC emissions data are from the GEIA inventory. Meteorological data were obtained from the Raleigh NWS, the ECMWF, and the NCEP/NCAR CDAS reanalysis project. We thank J. Eichinger (MCNC) and two anonymous reviewers for thoughtful criticism of this manuscript.

References

Allen, D. J., P. Kasibhatla, A. M. Thompson, R. B. Rood, B. G. Doddridge, K. E. Pickering, R. D. Hudson, and S.-J. Lin, Transport-induced interannual variability of carbon monoxide determined using a chemistry and transport model, *J. Geophys. Res.*, *101*, 28,655–28,669, 1996.

Anthes, R. A., A cumulus parameterization scheme utilizing a one-dimensional cloud model, *Mon. Weather Rev.*, *105*, 270–286, 1977.

Blackadar, A. K., Modeling the nocturnal boundary layer, paper presented at Third Symposium on Atmospheric Turbulence and Air Quality, Am. Meteorol. Soc., Raleigh, N. C., Oct. 19–22, 1976.

Bott, A., A positive definite advection scheme obtained by nonlinear renormalization of the advective fluxes, *Mon. Weather Rev.*, *117*, 1006–1015, 1989a.

Bott, A., Reply, *Mon. Weather Rev.*, *117*, 2633–2636, 1989b.

Brasseur, G., and S. Solomon, *Aeronomy of the Middle Atmosphere*, 2nd ed., 452 pp., D. Reidel, Norwell, Mass., 1986.

Brasseur, G., D. A. Hauglustaine, and S. Walters, Chemical compounds in the remote Pacific troposphere: Comparisons between MLOPEX measurements and chemical transport model calculations, *J. Geophys. Res.*, *101*, 14,795–14,813, 1996.

Byun, D., A. Hanna, C. Coats, and D. Hwang, Models-3 air quality model prototype science and computational concept development, in *Transactions of Air & Waste Management Association Specialty Conference on Regional Photochemical Measurement and Modeling Studies, San Diego, CA, November 8–12, 1993*, pp. 197–212, Air and Waste Manage. Assoc., Pittsburgh, Pa., 1995.

Chang, J. S., R. A. Brost, I.S.A. Isaksen, S. Madronich, P. Middleton, W. R. Stockwell, and C. J. Walcek, A three-dimensional acid deposition model: Physical concepts and formulation, *J. Geophys. Res.*, *92*, 14,681–14,700, 1987.

Chatfield, R. B., J. A. Vastano, L. Li, G. W. Sachse, and V. S. Connors, The great African plume from biomass burning: Generalizations from a three-dimensional study of TRACE A carbon monoxide, *J. Geophys. Res.*, in press, 1998.

Connors, V. S., T. Miles, and H. G. Reichle Jr., Large-scale transport of a CO-enhanced air mass from Europe to the Middle East, *J. Atmos. Chem.*, *9*, 479–496, 1989.

Crutzen, P. J., A discussion of the chemistry of some minor constituents in the stratosphere and troposphere, *Pure Appl. Geophys.*, *106–108*, 1385–1399, 1973.

Doddridge, B. G., P. A. Dirmeyer, J. T. Merrill, S. J. Oltmans, and R. R. Dickerson, Interannual variability over the eastern North Atlantic Ocean: Chemical and meteorological evidence for tropical influence on regional-scale transport in the extratropics, *J. Geophys. Res.*, *99*, 22,923–22,935, 1994.

Drummond, J. R., and G. S. Mand, The Measurements of Pollution in the Troposphere (MOPITT) instrument: Overall performance and calibration requirements, *J. Atmos. Oceanic Technol.*, *13*, 314–320, 1996.

Evans, W.F.J., and E. Puckrin, An observation of the greenhouse radiation associated with carbon monoxide, *Geophys. Res. Lett.*, *22*, 925–928, 1995.

Faluvegi, G. S., Modeling carbon monoxide transport during April of 1994, M. S. thesis, N. C. State Univ., Raleigh, 1997.

Grell, G., J. Dudhia, and D. Stauffer, A description of the fifth-generation Penn State/NCAR mesoscale model (MM5), *NCAR Tech. Note NCAR/TN-398+STR*, 117 pp., Natl. Cent. for Atmos. Res., Boulder, Colo., 1995.

Guenther, A., et al., A global model of natural volatile organic compound emissions, *J. Geophys. Res.*, *100*, 8873–8892, 1995.

Khalil, M.A.K., and R. A. Rasmussen, The global cycle of carbon monoxide: Trends and mass balance, *Chemosphere*, *20*, 227–242, 1990.

Kuo, H. L., Further studies of the parameterization of the effects of cumulus convection on large scale flow, *J. Atmos. Sci.*, *31*, 1232–1240, 1974.

Lin, X., F. Zaucker, E.-Y. Hsie, M. Trainer, and S. A. McKeen, Radon 222 simulations as a test of a three-dimensional regional transport model, *J. Geophys. Res.*, *101*, 29,165–29,177, 1996.

Logan, J. A., M. J. Prather, S. C. Wofsy, and M. B. McElroy, Tropospheric chemistry: A global perspective, *J. Geophys. Res.*, *86*, 7210–7254, 1981.

Luke, W. T., R. R. Dickerson, W. F. Ryan, K. E. Pickering, and L. J. Nunnermacker, Tropospheric chemistry over the lower Great Plains of the United States, 2, Trace gas profiles and distributions, *J. Geophys. Res.*, *97*, 20,647–20,670, 1992.

Müller, J.-F., Geographical distribution and seasonal variation of surface emissions and deposition velocities of atmospheric trace gases, *J. Geophys. Res.*, *97*, 3787–3804, 1992.

Müller, J.-F, and G. Brasseur, IMAGES: A three-dimensional chemical model of the global troposphere, *J. Geophys. Res.*, *100*, 16,445–16,490, 1995.

Newell, R. E., S. T. Shipley, V. S. Connors, and H. G. Reichle Jr., Regional studies of potential carbon monoxide sources based on space shuttle and aircraft measurements, *J. Atmos. Chem.*, *6*, 61–81, 1988.

Odman, M. T., and C. L. Ingram, Multi-scale Air Quality Simulation Platform (MAQSIP): Source code documentation and validation, *MCNC Tech. Rep. ENV-96TR002-v1.0*, 83 pp., N. C. Supercomput. Cent., Research Triangle Park, 1996.

Organization for Economic Cooperation and Development (OECD), *Environmental Data, Compendium 1989*, Paris, 1989.

Pacyna, J. M., and T. E. Graedel, Atmospheric emissions inventories: Status and prospects, *Annu. Rev. Energy Environ.*, *20*, 265–300, 1995.

Pickering, K. E., J. R. Scala, A. M. Thompson, W.-K. Tao, and J. Simpson, A regional estimate of convective transport of CO from biomass burning, *Geophys. Res. Lett.*, *19*, 289–292, 1992.

Pinto, J. H., Y. L. Yung, D. Rind, G. L. Russell, J. A. Lerner, J. E. Hansen, and S. Hameed, A general circulation model study of atmospheric carbon monoxide, *J. Geophys. Res.*, *88*, 3691–3702, 1983.

Pougatchev, N. S., and G. W. Sachse, Characterization of carbon monoxide measurements by gas filter correlation radiometers from satellites, in *Optical Remote Sensing of the Atmosphere, OSA Tech. Dig. Ser.*, vol. 5, pp. 122–124, Opt. Soc. of Am., Washington, D. C., 1997.

Reichle, H. G., Jr., V. S. Connors, J. A. Holland, W. D. Hypes, H. A. Wallio, J. C. Casas, B. B. Gormsen, M. S. Saylor, and W. D. Hesketh, Middle and upper tropospheric carbon monoxide mixing ratios as measured by a satellite-borne remote sensor during November 1981, *J. Geophys. Res.*, *91*, 10,865–10,887, 1986.

Reichle, H. G., Jr., V. S. Connors, J. A. Holland, R. T. Sherrill, H. A. Wallio, J. C. Casas, E. P. Condon, B. B. Gormsen, and W. Seiler, The distribution of middle tropospheric carbon monoxide during early October 1984, *J. Geophys. Res.*, *95*, 9845–9856, 1990.

Reichle, H. G., Jr., et al., Space shuttle based global CO measurements during April and October 1994, MAPS instrument, data reduction, and data validation, *J. Geophys. Res.*, this issue.

Seiler, W., and R. Conrad, Contributions of tropical ecosystems to the global budgets of trace gases especially CH_4, H_2, CO, and N_2O, in *Geophysiology of Amazonia*, edited by R. Dickinson, pp. 133–162, John Wiley, New York, 1987.

Sze, N. D., Anthropogenic CO emissions: Implications for the atmospheric CO-OH-CH_4 cycle, *Science*, *195*, 673–674, 1977.

Thompson, A. M., K. E. Pickering, R. R. Dickerson, W. G. Ellis Jr., D. J. Jacob, J. R. Scala, W.-K. Tao, D. P. McNamara, and J. Simpson, Convective transport over the central United States and its role in regional CO and ozone budgets, *J. Geophys. Res.*, *99*, 18,703–18,711, 1994.

Thompson, A. M., W.-K. Tao, K. E. Pickering, J. R. Scala, and J. Simpson, Tropical deep convection and ozone formation, *Bull. Am. Meteorol. Soc.*, *78*, 1043–1054, 1997.

U.S. Environmental Protection Agency (EPA), National air pollutant emission trends, 1900–1994, *Rep. EPA-454/R-95-011*, Washington, D. C., 1995.

Volz, A., D. H. Ehhalt, and R. G. Derwent, Seasonal and latitudinal variation of ^{14}CO and the tropospheric concentration of OH radicals, *J. Geophys. Res.*, *86*, 5163–5171, 1981.

Wang, Y., W.-K. Tao, K. E. Pickering, A. M. Thompson, R. Adler, J. Simpson, P. Keehn, and G. Lai, Mesoscale model (MM5) simulations of TRACE A and PRESTORM convective events and associated tracer transport, *J. Geophys. Res.*, *101*, 24,013–24,027, 1996.

Zhang, D.-L., and R. A. Anthes, A high-resolution model of the planetary boundary layer—Sensitivity tests and comparisons with SESAME-79 data, *J. Appl. Meteorol.*, *21*, 1594–1609, 1982.

K. Alapaty, V. S. Connors, G. S. Faluvegi (corresponding author), S. Raman, and H. G. Reichle Jr., Department of Marine, Earth, and Atmospheric Sciences, North Carolina State University, Jordan Hall Box 8208, Raleigh, NC 27695-8208. (e-mail: greg@maps.nrrc.ncsu.edu)

R. Mathur, Environmental Programs, MCNC-North Carolina Supercomputing Center, P.O. Box 12889, 3021 Cornwallis Rd., Research Triangle Park, NC 27709.

(Received February 10, 1998; revised August 11, 1998;
accepted September 9, 1998.)